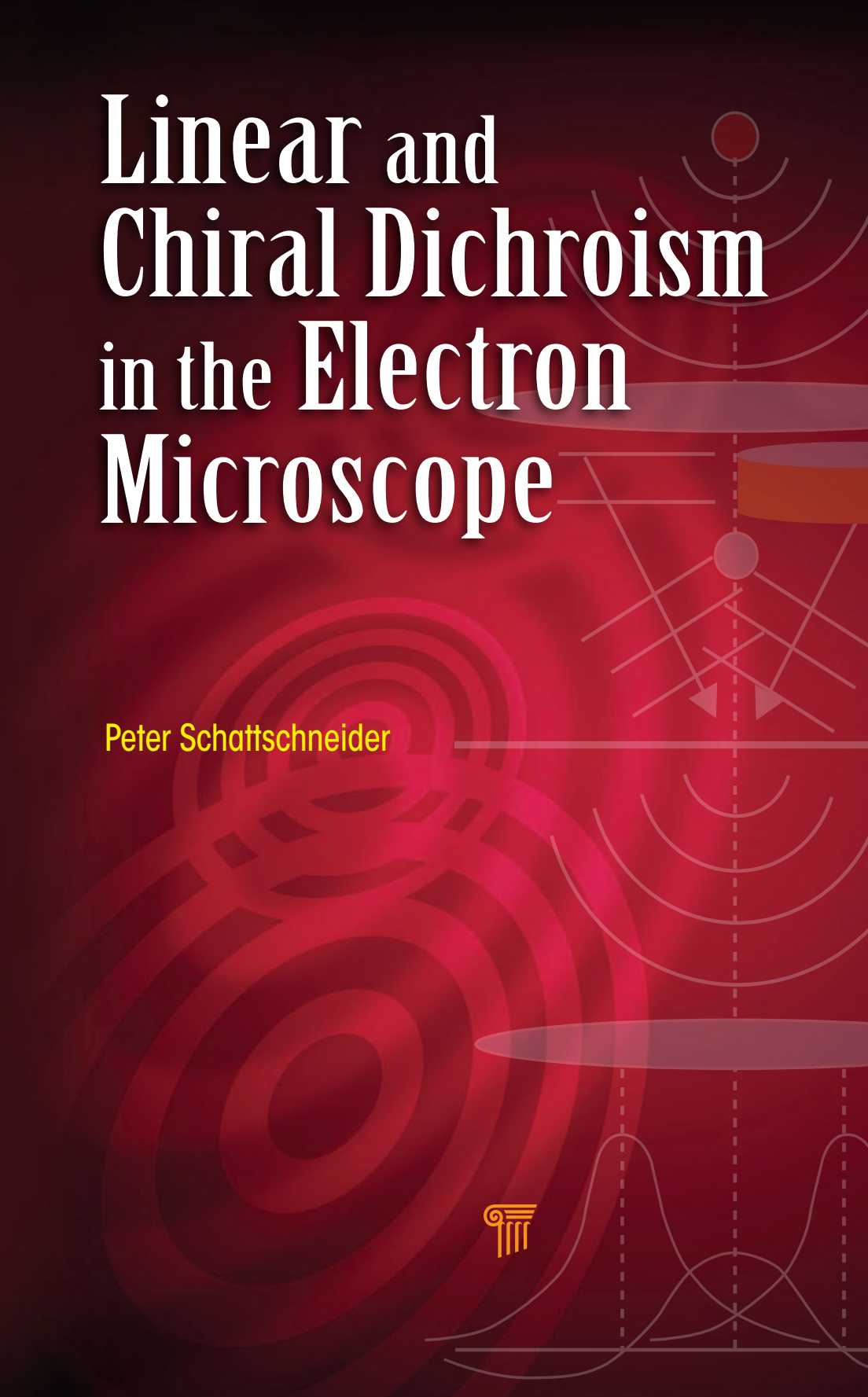


Linear and Chiral Dichroism in the Electron Microscope



Peter Schattschneider



**Linear and
Chiral Dichroism
in the Electron
Microscope**



This page intentionally left blank

Linear and Chiral Dichroism in the Electron Microscope



Peter Schattschneider

CRC Press
Taylor & Francis Group
6000 Broken Sound Parkway NW, Suite 300
Boca Raton, FL 33487-2742

© 2011 by Taylor & Francis Group, LLC
CRC Press is an imprint of Taylor & Francis Group, an Informa business

No claim to original U.S. Government works
Version Date: 20120201

International Standard Book Number-13: 978-9-81430-317-0 (eBook - PDF)

This book contains information obtained from authentic and highly regarded sources. Reasonable efforts have been made to publish reliable data and information, but the author and publisher cannot assume responsibility for the validity of all materials or the consequences of their use. The authors and publishers have attempted to trace the copyright holders of all material reproduced in this publication and apologize to copyright holders if permission to publish in this form has not been obtained. If any copyright material has not been acknowledged please write and let us know so we may rectify in any future reprint.

Except as permitted under U.S. Copyright Law, no part of this book may be reprinted, reproduced, transmitted, or utilized in any form by any electronic, mechanical, or other means, now known or hereafter invented, including photocopying, microfilming, and recording, or in any information storage or retrieval system, without written permission from the publishers.

For permission to photocopy or use material electronically from this work, please access www.copyright.com (<http://www.copyright.com/>) or contact the Copyright Clearance Center, Inc. (CCC), 222 Rosewood Drive, Danvers, MA 01923, 978-750-8400. CCC is a not-for-profit organization that provides licenses and registration for a variety of users. For organizations that have been granted a photocopy license by the CCC, a separate system of payment has been arranged.

Trademark Notice: Product or corporate names may be trademarks or registered trademarks, and are used only for identification and explanation without intent to infringe.

Visit the Taylor & Francis Web site at
<http://www.taylorandfrancis.com>

and the CRC Press Web site at
<http://www.crcpress.com>

Preface

Energy loss magnetic chiral dichroism (EMCD) is a rather new application that can detect element specific magnetic moments of solids in the electron microscope. The method is based on the analysis of ionisation edges in electron energy loss spectra (EELS), similar to X-ray magnetic circular dichroism (XMCD) in the synchrotron. EMCD was predicted in 2003 and experimentally verified in 2006. Compared to XMCD this was a very rapid development. Although ionisation edges in EELS (where the sensitivity to magnetic transitions is evident in retrospect) are well understood the discovery of EMCD came as a surprise to the community.

We know now from theory and simulations that *in principle* everything that can be done in the synchrotron is also feasible in an electron microscope. The caveat lies in the *italics*; there are many obstacles in taking a dichroic energy loss spectrum that do not exist for synchrotron radiation. At the focus of these obstacles is the probe electron which reveals its difficult character here — it interacts stronger with matter, it is a Fermion, and it is more difficult to handle than a photon is. As a consequence, there are significant differences between EMCD and XMCD in spite of the similar theoretical description. In technical terms, these differences relate to the short extinction length for electron scattering on the crystal lattice, and to the high spatial resolution of electron microscopy. Recently, a resolution of about 1 nm in EMCD was demonstrated; the details are discussed in Chapter 12 of this monograph.

The intrinsic advantage of sub-nm resolution in electron microscopy allows new and exciting insights into the behaviour of electron spins and their interaction, a fact that is difficult to exploit because of the extremely faint signal. But EMCD is in rapid evolution. With new monochromators, aberration correctors and novel concepts for energy filters, pioneered by Harald Rose and others, the situation has improved. At the time of writing there are promising experiments under way in order to map spins of single atomic columns.

There has been so much progress in the last years that we (the authors of the following chapters and the publisher) considered the subject mature enough to present it to a broader audience. On second thoughts it became clear that the whole subject of symmetry breaking in EELS merits publication. It seemed appropriate to cover also aspects of anisotropy in EELS, both from an experimental and a theoretical point of view.

There are many open problems, such as the notoriously low L_2 signal which is not well understood. But now that the fundamental features of the method are well established it can be applied to real problems; most of them will be related to interfaces and nanoparticles. This is not so clear for another case of broken symmetry, namely linear dichroism in EELS; here, applications will probably focus

on the anisotropy of the density of states in larger systems (with examples given in Chapter 1), and on avoiding directional dependence of ionisation edges by use of the magic angle conditions, discussed in Chapter 7.

The book is organized as follows: the first three chapters are devoted to the basic principles of anisotropy and chirality, including an introduction to the XMCD technique. Chapters 4 to 8 cover the theory and numerics of the simulation of dichroic XMCD and EMCD spectra, as well as two aspects of symmetry breaking that are both theoretically demanding and important for the interpretation of experiments: the magic angle and the application of sum rules. Chapters 9 to 11 deal with the practical aspects of EMCD, such as the different techniques, data treatment, noise problems, the role of the crystal lattice, and typical applications. The final three chapters cover some newer aspects of EMCD that resulted from the refinement of experimental techniques and interpretation. For example, the problem of mapping magnetic moments in a lattice is intimately connected with Bragg scattering on that lattice. Is it then realistic to hope for spin maps on the atomic scale? Here, the chapter on magnetic X-ray holography, an elegant technique that holds promise for high resolution magnetic mapping, is well placed. Its penultimate position restores the broken symmetry with respect to the first part where XMCD was introduced.

I do hope that the reader will profit in several ways from this monograph — in conceiving new experiments in electron microscopy, in a better understanding of symmetry breaking in EELS, in combining EMCD with XMCD, and — maybe most importantly — in soliciting efforts to improve EMCD with the aim to make electron spins in the solid directly visible on the atomic scale.

P. Schattschneider
Vienna, March 2011

Foreword

It is more than seventy years since Siemens put the first commercial transmission electron microscope on the market. Over the decades, that first design has been improved by the inclusion of extra lenses and more coherent sources. Numerous accessories have joined the original instrument: stigmators, in-column and post-column energy analysers and, more recently, electron biprisms, monochromators and aberration correctors. New ways of using the microscope have emerged: Lorentz microscopy, the various holographic modes and of course the extensive family of diffraction techniques. Just occasionally, it is suddenly realised that, with no major modification, the electron microscope can detect physical phenomena that had seemed beyond its reach. The subject of this book is a striking example of such a revelation. Magnetic circular dichroism, which can be detected with X-rays, had been thought to be invisible to (unpolarized) electrons. But in 2003, Cécile Hébert and the editor of this book, Peter Schattschneider, suggested that this was not inevitable and a few years later, their prediction was confirmed experimentally. Circular dichroism can be detected in electron energy-loss spectra by a most ingenious manipulation of the experimental conditions. Full details of this and some related topics are provided in the chapters that follow and it is no part of my role to recapitulate them. What I do wish to emphasize is that the development of new techniques such as this requires an unusual (and often winning) combination of skills. Mastery of the theory of image formation and, in particular, of the theory of scattering in crystalline specimens is essential but not sufficient. To this must be added a good knowledge of the optics of the microscope and its accessories, notably, the interplay between the microscope lenses and the spectrometer. It is the marriage between these skills, not often united in a single individual, that leads to such developments. A comparable case is seen in ptychography. First suggested by the late Walter Hoppe, who was very familiar with TEM optics and the phase problem, and who was probably the first to realise that the STEM was well adapted for ptychography, it was subsequently made practical for the STEM by John Rodenburg, inspired by Richard Bates's instinct to Fourier transform everything in sight in difficult situations. Here again, we have an extremely original development, resulting from the union of the same two areas of expertise, instrumentation and image-formation theory.

This combination of skills, although vital for the discovery of new techniques, is fortunately not essential for the reader. Those who are closer to instrumental developments will enjoy the ingenious ways in which illumination conditions, specimen alignment and orientation relative to the spectrometer are juggled to yield signals strong enough to be detected while those primarily interested in

the materials science of magnetic specimens will appreciate the information that emerges and will no doubt attempt to apply the technique to their own specimens; and there is plenty of intriguing material for the theoreticians as well.

The experimental procedures have evolved considerably in the past few years and the whole subject is now mature enough to merit publication of this collection of essays on linear and circular magnetic dichroism. The authors of these contributions have collaborated in many of the published accounts with the result that the material is presented in a homogeneous fashion, doubtless largely thanks to the editor's influence.

I was asked to write a Foreword, not a "Forechapter", and it is therefore time for me to stop and to urge you to launch into this fascinating collection.

Peter Hawkes
Toulouse, May 2011

Acknowledgments

Lionel Calmels acknowledges Marie-Anne Arrio (IMPMC-Paris) for useful discussions on the atomic multiplet theory.

The authors of chapter 5 appreciate partial support from the European Theoretical Spectroscopy Facility (ETSF), and from the Italian Ministero per l'Istruzione, l'Universit  e la Ricerca (MIUR) through project PRIN/COFIN, contract 2008NX9Y7.

The authors of chapter 6 gratefully acknowledge the many contributions of A. L. Ankudinov to this work. This research is supported in part by the DFG and BMBF (HW), by US DOE Grant DE-FG03-97ER45623 (JJR), and was facilitated by the DOE BES Computational Materials and Chemical Sciences Network (CMCSN).

The authors of chapter 8 gratefully acknowledge contributions and suggestions from A. Ankudinov, A. Nesvizhskii, Peter Oppeneer, Olle Eriksson, and Pavel Novak. This work was supported in part by Swedish Research Council (JR), DOE BES Grant DE-FG03-97ER45623 (JJR) and was facilitated by the DOE CMSN.

The authors of chapter 10 would like to acknowledge the Swedish Science Foundation and STINT for their support of this work.

S. Eisebitt likes to thank Dr. Olav Hellwig (Hitachi Global Storage Technologies, San Jose Research Center, USA) and Prof. Dr. Manfred Albrecht (Chemnitz University of Technology) for collaborative work on the imaging of patterned magnetic storage media which has led to the examples presented in Fig. 13.6.

The authors of chapter 14 gratefully acknowledge financial support of the Austrian Science Fund (FWF): I-543-N20.

The editor wants to thank friends and relatives for their patience during the editorial work, many colleagues for enlightening discussions, and Mischa Nelhiebel for his thesis wherein the EMCD effect lay dormant for many years.

This page intentionally left blank

Contents

| | |
|---|-----------|
| <i>Preface</i> | v |
| <i>Foreword</i> | vii |
| <i>Acknowledgments</i> | ix |
| <i>Acronyms</i> | xv |
| Chapter 1 Anisotropy in Electron Energy Loss Spectrometry | 1 |
| 1.1 Introduction | 1 |
| 1.2 Interaction between a pair of electrons | 2 |
| 1.3 Fermi's golden rule | 4 |
| 1.4 The double differential scattering cross section | 6 |
| 1.5 The dipole approximation | 7 |
| 1.6 Scattering kinematics | 11 |
| 1.7 Experimental considerations | 12 |
| 1.8 Conclusion | 20 |
| Chapter 2 The Principles of XMCD and Its Application to L-Edges in Transition Metals | 23 |
| 2.1 Introduction | 23 |
| 2.2 Experimental details | 23 |
| 2.3 The absorption coefficient and its magnetic part | 26 |
| 2.4 Origin of XMCD in a simple two-step model | 27 |
| 2.5 General formulation via the sum rules | 33 |
| 2.6 Magnetic X-ray microscopy | 36 |
| 2.7 Summary | 40 |
| Chapter 3 Chirality in Electron Energy Loss Spectrometry | 43 |
| 3.1 Broken symmetries in EELS | 43 |
| 3.2 The effective photon | 44 |
| 3.3 Inelastic interference | 47 |
| 3.4 The mixed dynamic form factor | 50 |
| 3.5 Properties of the MDFF | 52 |

| | | |
|------------------|--|------------|
| 3.6 | Equivalence to X-ray dichroism | 55 |
| 3.7 | Experimental setup | 57 |
| 3.8 | Chirality of transitions | 62 |
| Chapter 4 | Momentum-resolved ELNES and EMCD of $L_{2,3}$ Edges from the Atomic Multiplet Theory | 65 |
| 4.1 | Core level spectroscopy of transition metal oxides and strongly correlated materials | 65 |
| 4.2 | Atomic multiplet theory for the calculation of X-ray absorption spectra | 66 |
| 4.3 | Parameters for an atomic multiplet calculation | 69 |
| 4.4 | Momentum-resolved EELS and EMCD spectra from the atomic multiplet theory | 69 |
| 4.5 | EELS and EMCD spectra at the $L_{2,3}$ edge of IRON in magnetite | 72 |
| 4.6 | Conclusions | 76 |
| Chapter 5 | XMCD Spectra Based on Density Functional Theory | 79 |
| 5.1 | Introduction | 79 |
| 5.2 | Density functional theory | 79 |
| 5.3 | The linearized augmented plane wave method | 81 |
| 5.4 | XMCD | 82 |
| 5.5 | Results | 86 |
| 5.6 | Conclusions | 96 |
| Chapter 6 | Multiple-Scattering Theory and Interpretation of XMCD | 101 |
| 6.1 | Multiple-scattering theory of XMCD | 101 |
| 6.2 | Applications to XMCD | 103 |
| 6.3 | Examples: Rare earth metals | 106 |
| 6.4 | Conclusions | 112 |
| Chapter 7 | Linear Dichroism and the Magic Angle | 115 |
| 7.1 | Relativistic effects | 115 |
| 7.2 | The Magic Angle | 122 |
| 7.3 | Conclusion | 126 |
| Chapter 8 | Sum Rules in EMCD and XMCD | 129 |
| 8.1 | Operator expansion approach and XMCD sum rules | 130 |
| 8.2 | Error sources in XMCD sum rules | 131 |
| 8.3 | Simplified derivation of EMCD sum rules | 132 |

| | | |
|--|---|------------|
| 8.4 | Rotationally invariant form of the EMCD sum rules | 135 |
| 8.5 | Sum rules for real part of MDFFs | 141 |
| 8.6 | Dipole allowed sum rules for ELNES spectra — summary | 142 |
| 8.7 | Error sources in EMCD sum rules | 143 |
| Chapter 9 EMCD Techniques | | 149 |
| 9.1 | Basic geometry for EMCD | 150 |
| 9.2 | Tilt series | 154 |
| 9.3 | Detector shift | 155 |
| 9.4 | Objective aperture shift | 158 |
| 9.5 | Convergent beam methods | 159 |
| 9.6 | Chiral STEM | 163 |
| 9.7 | The q vs. E diagram | 164 |
| 9.8 | Chiral EFTEM | 165 |
| 9.9 | Considerations on the convergence and collection angles | 169 |
| 9.10 | Conclusions | 170 |
| Chapter 10 Artefacts and Data Treatment in EMCD Spectra | | 175 |
| 10.1 | Artefacts in the data cube | 176 |
| 10.2 | Data treatment | 185 |
| 10.3 | Conclusion | 195 |
| Chapter 11 The Role of the Crystal in EMCD | | 197 |
| 11.1 | The Bloch wave formalism | 197 |
| 11.2 | The density matrix formalism | 199 |
| 11.3 | Density matrices in the electron microscope | 200 |
| 11.4 | Simulating the inelastic diffraction pattern | 202 |
| 11.5 | Obtaining the EMCD signal | 206 |
| 11.6 | Simulation results | 207 |
| 11.7 | Recommendations for experiments | 209 |
| Chapter 12 EMCD on the Nanometre Scale | | 213 |
| 12.1 | Introduction | 213 |
| 12.2 | EMCD in the STEM | 214 |
| 12.3 | Serial STEM-EMCD | 217 |
| 12.4 | Parallel STEM-EMCD | 220 |
| 12.5 | Conclusion | 222 |

| | | |
|-------------------|--|------------|
| Chapter 13 | Magnetic Dichroism in X-ray Holography | 225 |
| 13.1 | Overview | 225 |
| 13.2 | Holography with soft X-rays | 227 |
| 13.3 | Holographic imaging of magnetic domains | 232 |
| 13.4 | Recent developments and outlook | 237 |
| Chapter 14 | Prospects for Spin Mapping with Atomic Resolution | 243 |
| 14.1 | Mapping of single spins | 243 |
| 14.2 | Prospects for sub-lattice resolution in EMCD | 247 |
| 14.3 | Angular momentum in EELS | 250 |
| | <i>Index</i> | 257 |

Acronyms

| | |
|---------|---|
| AFM: | Atomic Force Microscope; |
| CBED: | Convergent Beam Electron Diffraction; |
| CCD: | Charge-Coupled Device; |
| CD: | Circular Dichroism; |
| DDSCS: | Double Differential Scattering Cross Section; |
| DFF: | Dynamic Form Factor; |
| DFT: | Density Functional Theory; |
| DoS: | Density of States; |
| EDX: | Energy Dispersive X-ray spectroscopy/analysis; |
| EELS: | Electron Energy Loss Spectrometry; |
| EFS: | Energy Filtered Series; |
| EFTEM: | Energy-Filtered Transmission Electron Microscopy; |
| ELNES: | Energy Loss Near Edge Structure; |
| EMCD: | Energy-loss Magnetic Chiral Dichroism; |
| ESD: | Energy Spectroscopic Diffraction; |
| FWHM: | Full Width at Half Maximum; |
| HWHM: | Half Width at Half Maximum; |
| HOLZ: | High Order Laue Zone; |
| LACDIF: | Large Angle Convergent DIFfraction; |
| LCC: | Laue Circle Center; |
| LCP: | Left-hand Circular Polarization; |
| LDoS: | Local(projected) DoS; |
| MCD: | Magnetic Circular Dichroism; |
| MLD: | Magnetic Linear Dichroism; |
| MOKE: | Magneto-Optic Kerr Effect; |
| MDF: | Mixed Dynamic Form Factor; |
| PEEM: | Photo Emission Electron Microscopy; |
| RCP: | Right-hand Circular Polarization; |
| SAA: | Selected Area Aperture; |
| SEA: | Spectrometer Entrance Aperture; |

| | |
|-------------|--|
| SEM: | Scanning Electron Microscope; |
| SNR or S/N: | Signal-to-Noise Ratio; |
| STEM: | Scanning Transmission Electron Microscope; |
| STM: | Scanning Tunneling Microscope; |
| STXM: | Scanning Transmission X-ray Microscope; |
| TEM: | Transmission Electron Microscope; |
| XAS: | X-ray Absorption Spectrometry; |
| XMCD: | X-ray Magnetic Circular Dichroism; |
| XNCD: | X-ray Natural Circular Dichroism; |
| ZLP: | Zero Loss Peak. |

Chapter One

Anisotropy in Electron Energy Loss Spectrometry

C. Hébert, J. C. Le Bossé, G. A. Botton and P. Schattschneider

1.1 INTRODUCTION

In an electron energy loss spectrometry (EELS) experiment in a transmission electron microscope (TEM), fast electrons (in general 80 to 300 keV) are used as probe particles. Their kinetic energy corresponds to electron velocities of 50 to 80% of the light velocity. One would expect to see relativistic effects in the experiment. Surprisingly, apart of the replacement of the electron's rest mass by the relativistic mass, the non-relativistic quantum mechanical expressions for the scattering process hold in the majority of cases.¹ The incoming electron is almost exclusively considered as a plane wave. This fast electron may lose energy via interactions with the sample. For instrumental reasons, the energy range accessible is situated between 0 and at most 3000 to 4000 eV, with an energy resolution of 0.1 to 0.2 eV on a monochromated TEM [Egerton (2009)] and 0.7–0.8 eV on a conventional instrument with a field emission source. Phonon scattering is not accessible via EELS since the energy loss is far too small and these events are detected together with the very intense peak of the elastic scattering; they are called quasi-elastic. Therefore the events accessible are only electron-electron scattering events. Such events are referred to as *inelastic* as the internal energy of the target is changed. Figure 1.1 shows a schematic diagram of the possible scattering events together with an EELS spectrum.

Inelastic in the quantum mechanical sense means that the target wave function changes during the interaction. This distinguishes it from elastic scattering where the target remains in the same quantum mechanical state. Strictly speaking, this is never true since when only momentum is transferred, e.g. in a Bragg scattering event, the target changes momentum, and this necessarily means that its wave

¹This approximation is not valid any more for anisotropic systems because the Lorentz contraction breaks the spherical symmetry of the Coulomb potential. This aspect is treated in Chapter 7.

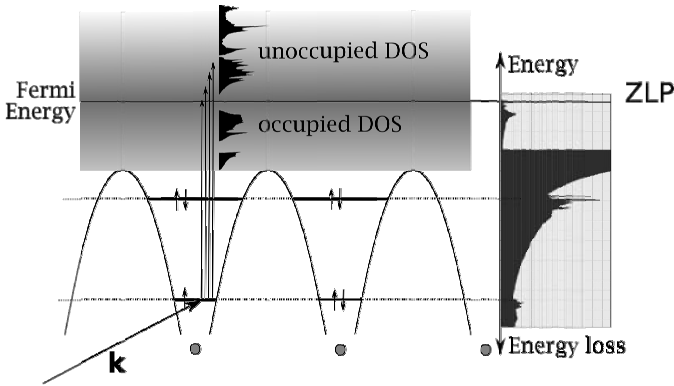


Figure 1.1 An EELS experiment records the energy lost by a fast incoming electron when it scatters inelastically against an electron of the sample. The sample's core electron then gains energy and is transferred to an empty state, above the Fermi level, while the fast electron loses the corresponding energy. The fine structures that can be seen after the ionisation edge mirrors the site and angular-momentum projected density of unoccupied states.

function changes. Only if we assume that the target can be described by a potential (caused by a rigid, infinitely heavy distribution of charges) is the elastic approach valid. In the present context inelastic means that the electronic subsystem changes its wave function.

As a consequence of the accessible energy losses, the outgoing electron has a velocity of the same order of magnitude as the incoming electron.

In the general case the fast electron can be considered as travelling through a medium of complex dielectric tensor (polarizability) ϵ and the double differential scattering cross section (DDSCS) for a given energy loss is linked to the loss function $\Im(-1/\epsilon)$ [Pines (1964); Egerton (1986); Schattschneider (1986)].

In the following we will consider the case where the energy loss $E = \hbar\omega$ is relatively large (above 100 eV) because the fast incoming electron scatters against a core electron of the sample. In this case, the real part of the dielectric tensor, $\epsilon_1(\omega)$, is close to 1 and the imaginary part, $\epsilon_2(\omega)$, is close to 0, therefore the screening term disappears and the DDSCS is proportional to ϵ_2 . The collective behaviour of the electron gas can be neglected and the process treated as an electron/electron scattering event.

1.2 INTERACTION BETWEEN A PAIR OF ELECTRONS

Core loss EELS events can be treated within a first order perturbation theory derived from the Born approximation. We consider a system which consists of a fast incident electron and a target electron immersed in a crystal potential. The

two-electron Hamiltonian of this system is given by

$$\hat{H} = \frac{\hat{\mathbf{p}}^2}{2m} + V_c(\mathbf{r}) + V_c(\mathbf{R}) + \frac{\hat{\mathbf{P}}^2}{2m} + U(\mathbf{r} - \mathbf{R}); \quad (1.1)$$

\mathbf{r} and \mathbf{p} denote the position and the momentum of the electron inside the target specimen, \mathbf{R} and \mathbf{P} denote the position and the momentum of the fast incident electron. The potential energy V_c describes the interaction of an electron with the atoms of the target. The interaction between the target electron and the fast incident electron is given by the Coulombic interaction:

$$U(\mathbf{r} - \mathbf{R}) = \frac{1}{4\pi\epsilon_0} \frac{e^2}{\|\mathbf{r} - \mathbf{R}\|}. \quad (1.2)$$

Long before the electron collision, when $\|\mathbf{r} - \mathbf{R}\|$ is very large compared with the target size, the state of the fast electron is assumed to be a solution of ²

$$\left(\frac{\hat{\mathbf{P}}^2}{2m} + V_c(\mathbf{R}) \right) |\mathbf{k}\rangle = E_{\mathbf{k}} |\mathbf{k}\rangle. \quad (1.3)$$

As the atomic potentials have a very weak contribution outside the target, they can be neglected and the solutions of the Schrödinger equation are plane waves. The electronic states of the target electron are a solution of

$$\left(\frac{\hat{\mathbf{p}}^2}{2m} + V_c(\mathbf{r}) \right) |\phi_j\rangle = E_j |\phi_j\rangle. \quad (1.4)$$

In other words, both electrons do not interact with each other and the state of the system is ³:

$$|\Psi_i\rangle = |\mathbf{k}\rangle \otimes |\phi_i\rangle. \quad (1.5)$$

When both electrons approach each other, the Coulombic interaction between them increases and can induce a transition from $|\Psi_i\rangle$ to a new state $|\Psi_f\rangle$ that we may call the final state of the system when the two electrons are again far apart. Target and probe states become entangled by the interaction and in general cannot be separated any more. The entangled state can be expanded into eigen functions $|\phi_j\rangle$ of the formerly isolated target

$$|\Psi_f\rangle = \sum_j |j\rangle \otimes |\phi_j\rangle. \quad (1.6)$$

The new eigen functions of the probe subsystem are not plane waves any longer, but we can expand them into plane waves

$$|j\rangle = \sum_k c_{jk} |\mathbf{k}\rangle. \quad (1.7)$$

²This state should actually be a solution of the Dirac equation, but we can neglect its spinorial nature as we are only interested in the fact that the fast electron loses a part of its kinetic energy.

³This approximation amounts to neglecting the exchange interaction between both electrons. It can be shown that this force is truly negligible.

Although the combined system is still in a pure state $|\Psi_f\rangle$ none of its subsystems can be described by a wave function [Landau (1977)]. Ignoring the information from the rest of the system leads to the description of the subsystem (the probe) by its reduced density matrix:

$$\rho_k = \text{Tr}_\Phi [|\Psi_f\rangle\langle\Psi_f|]. \quad (1.8)$$

Tr_Φ is the trace operation over the Φ subsystem (the target). Inserting Eq. (1.6), Eq. (1.7) into Eq. (1.8) one obtains

$$\rho_k = \sum_l \sum_{jj'kk'} c_{jk} c_{j'k'}^* \langle\phi_l|\phi_j\rangle\langle\phi_{j'}|\phi_l\rangle \otimes |\mathbf{k}\rangle\langle\mathbf{k}'|. \quad (1.9)$$

The probability of finding the probe in state $|\mathbf{k}_f\rangle$ is $\rho_k(\mathbf{k}_f) = \langle\mathbf{k}_f|\rho_k|\mathbf{k}_f\rangle$. By virtue of orthogonality

$$\rho_k(\mathbf{k}_f) = \sum_l |c_{lk_f}|^2. \quad (1.10)$$

It is instructive to observe that (by definition, Eq. 1.6 and 1.7)

$$|c_{lk}|^2 = |\langle\mathbf{k}|\otimes\langle\phi_l|\Psi_f\rangle|^2. \quad (1.11)$$

This is the probability of finding the probe in state $|\mathbf{k}\rangle$ and the target in state $|\phi_l\rangle$ after interaction. Since in general no closed solutions exist for the transition coefficients c_{lk} they are conveniently calculated in first order perturbation theory, applying Fermi's golden rule.

1.3 FERMI'S GOLDEN RULE

The transition rate (probability per unit of time to observe a transition from $|\Psi_i\rangle = |\mathbf{k}\rangle \otimes |\phi_i\rangle$ to $|\mathbf{k}'\rangle \otimes |\phi_l\rangle$) is

$$\frac{dW}{dt} = \frac{2\pi}{\hbar} |\langle\phi_l|\otimes\langle\mathbf{k}|U(\mathbf{r}-\mathbf{R})|\mathbf{k}'\rangle\otimes|\phi_i\rangle|^2 \delta(E_i + E_{\mathbf{k}} - E_l - E_{\mathbf{k}'}). \quad (1.12)$$

The matrix element in the above expression can be simplified when observing the plane wave property of the probe subsystem and inserting Eq. (1.2) [Bethe 1930]. We get

$$\langle\phi_l|\otimes\langle\mathbf{k}|U(\mathbf{r}-\mathbf{R})|\mathbf{k}'\rangle\otimes|\phi_i\rangle = \frac{e^2}{\epsilon_0\Omega_0q^2} \langle\phi_l|e^{i\mathbf{q}\cdot\mathbf{r}}|\phi_i\rangle. \quad (1.13)$$

In this expression, ϵ_0 is the vacuum dielectric permittivity, Ω_0 is the volume of the box in which the periodic boundary conditions are applied and q is the modulus of

$$\mathbf{q} = \mathbf{k}' - \mathbf{k} \quad (1.14)$$

where \mathbf{k}' is the wave vector of the fast electron when it exits the sample. $-\hbar\mathbf{q}$ is therefore the momentum transferred from the fast electron to the target electron.

The scattering geometry is pictured in Fig. 1.4. By using 1.13, the expression 1.12 of the transition probability per unit of time can be transformed into

$$\frac{dW}{dt} = \frac{2\pi e^4}{\hbar \epsilon_0^2 \Omega_0^2} \frac{1}{q^4} \left| \langle \phi_i | e^{i\mathbf{q}\cdot\mathbf{r}} | \phi_l \rangle \right|^2 \delta(E_i + E_{\mathbf{k}} - E_f - E_{\mathbf{k}+\mathbf{q}}). \quad (1.15)$$

Actually, we are interested in the transition rate to a group of states

$$|\Psi\rangle = \sum_{\mathbf{k}' \in \Delta} |\mathbf{k}'\rangle \otimes |\phi_l\rangle \quad (1.16)$$

selected by the electron collector. So, we must consider

$$\frac{dW}{dt} = \frac{2\pi e^4}{\hbar \epsilon_0^2 \Omega_0^2} \sum_{\mathbf{k}' \in \Delta} \frac{|\langle \phi_i | e^{i\mathbf{q}\cdot\mathbf{r}} | \phi_l \rangle|^2}{q^4} \delta(E_i + E_{\mathbf{k}} - E_l - E_{\mathbf{k}+\mathbf{q}}). \quad (1.17)$$

If Ω_0 goes to infinity, then the summation over \mathbf{k}' can be transformed into an integral over \mathbf{k}' :

$$\frac{1}{\Omega_0} \sum_{\mathbf{k}' \in \Delta} \longrightarrow \iiint_{\Delta} \frac{d^3\mathbf{k}'}{(2\pi)^3}.$$

Moreover, the integration over \mathbf{k}' can be carried out by using spherical coordinates,

$$d^3\mathbf{k}' = k'^2 \sin\theta' d\theta' d\varphi' dk' = k'^2 d\Omega' dk'.$$

In this expression, $d\Omega'$ is the element of solid angle in the direction of \mathbf{k}' . Here, the relativistic energy of the fast electron is used:

$$E_{\mathbf{k}'}^2 = c^2 p'^2 + m^2 c^4 \quad (1.18)$$

instead of the classical expression of its kinetic energy. As a consequence

$$\begin{aligned} E_{\mathbf{k}'} dE_{\mathbf{k}'} &= c^2 p' dp' \\ &= \hbar^2 c^2 k' dk'. \end{aligned}$$

Actually, $E_{\mathbf{k}'} = m\gamma' c^2$, and thus

$$k'^2 dk' = \frac{m\gamma'}{\hbar^2} k' dE_{\mathbf{k}'}. \quad (1.19)$$

Let us remark that the use of the relativistic expression of the electron energy introduces the factor

$$\gamma' = \frac{1}{\sqrt{1 - \frac{v'^2}{c^2}}} \quad (1.20)$$

which depends on the fast electron velocity v' , after the electron/target collision.

By using the Bohr radius

$$a_0 = \frac{4\pi\epsilon_0 \hbar^2}{me^2} \quad (1.21)$$

the transition probability can be rewritten in the form

$$\frac{dW}{dt} = \frac{4\hbar}{m\Omega_0 a_0^2} \quad (1.22)$$

$$\times \iiint_{\Delta} \gamma' k' \frac{|\langle \phi_i | e^{i\mathbf{q}\cdot\mathbf{r}} | \phi_l \rangle|^2}{q^4} \delta(E_i + E_{\mathbf{k}} - E_l - E_{\mathbf{k}+\mathbf{q}}) d\Omega' dE_{\mathbf{k}'}$$

This expression defines the probability of transition from the core state $|\phi_i\rangle$ to the final state $|\phi_l\rangle$, per unit of time, and per unit of solid angle, per unit of energy, when the fast incident electron is detected in the direction of the wave vector \mathbf{k}' .

1.4 THE DOUBLE DIFFERENTIAL SCATTERING CROSS SECTION

The transition probability $|c_{lk}|^2$, Eq. (1.11) is obtained by dividing the transition rate Eq. (1.22) by the incident particle current $\hbar k / (m\gamma\Omega_0)$. Then, we have [Hébert and Schattschneider (2003)]

$$W = |c_{lk}|^2 = \frac{4\gamma\gamma' k'}{a_0^2 k} \frac{|\langle \phi_i | e^{i\mathbf{q}\cdot\mathbf{r}} | \phi_l \rangle|^2}{q^4} \delta(E_i + E - E_l). \quad (1.23)$$

Here $\hbar\mathbf{q}$, given by 1.14, is the momentum transferred from the incident electron to the target and

$$E = E_{\mathbf{k}} - E_{\mathbf{k}+\mathbf{q}} \quad (1.24)$$

is the energy loss of the fast incident electron. With the proper normalisation volume ρ_k is identical to the double differential scattering cross section (DDSC) [Schattschneider (1999)]

$$\frac{\partial^2 \sigma}{\partial E \partial \Omega} = \rho_k(\mathbf{k}') = \sum_l |c_{lk'}|^2.$$

For a Fermionic system, only transitions to unoccupied states are allowed in the sum over l resulting in a subset denoted by the index j . According to these remarks and inserting equation (1.23) the DDSCS reduces to the expression

$$\frac{\partial^2 \sigma}{\partial E \partial \Omega} = \frac{4\gamma\gamma' k'}{a_0^2 q^4 k} S(\mathbf{q}, E) \quad (1.25)$$

in which the dynamic form factor (DFF) is given by:

$$S(\mathbf{q}, E) = \sum_{j \text{ unoc}} \left| \langle \phi_i | e^{i\mathbf{q}\cdot\mathbf{r}} | \phi_j \rangle \right|^2 \delta(E_i + E - E_j). \quad (1.26)$$

The ratio k'/k is very close to 1 because the energy loss, E , is small compared with the kinetic energy of the incident electron. For the same reason, the fast

electron velocity after the collision (v') and before the collision (v) are very close, and thus $\gamma' \approx \gamma$. Therefore the DDSCS is often found as:

$$\frac{\partial^2 \sigma}{\partial \Omega \partial E} = \frac{4\gamma^2}{a_0^2 q^4} S(\mathbf{q}, E) \quad (1.27)$$

The $|\phi_i\rangle$ and $|\phi_f\rangle$ states represent the initial and final one-electron states. In the general case where the target is composed of a large number of atoms, it is not possible to write them explicitly. The wave functions which described the initial core atomic states can be calculated by using various approximations ranging from hydrogen-like to Slater-type orbitals. The unoccupied one-electron valence states can be described with wave functions calculated from ready-to-use program packages such as WIEN2k, FEFF or CASTEP [Rez and Muller (2008)]. The matrix elements in 1.25 are evaluated from these wave functions. Figure 1.2 shows an example of experimental and calculated O-K fine structures in various vanadium oxides [Hébert *et al.* (2002)]. For a review of methods for calculating EELS spectra, see [Rez *et al.* (1999); Rez and Muller (2008)].

1.5 THE DIPOLE APPROXIMATION

Let us choose the coordinate system in such a way that the origin is located at the probed atom site. Then, the core atomic wave function, $\phi_i(\mathbf{r})$, extends in a small region localized around the origin, and the modulus of the \mathbf{r} vector, r , remains small compared with the sample size. On the other hand, the modulus q of the

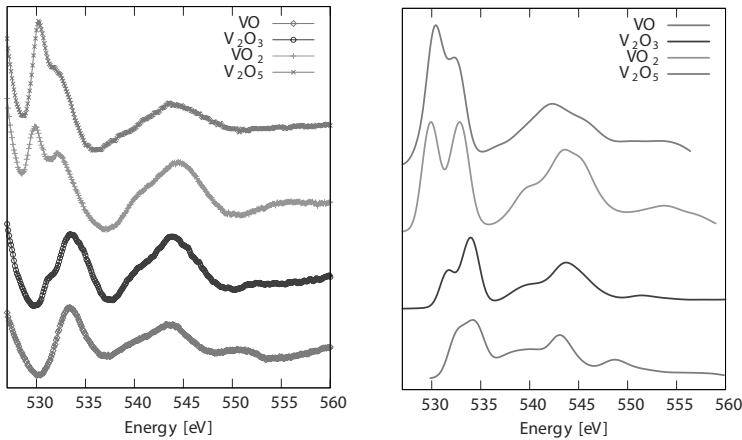


Figure 1.2 Experimental (left) and calculated (right) O-K edges fine structures in various vanadium oxides. The calculations was performed with the WIEN2k code. Spectra are shifted vertically for better visibility, starting with VO (bottom) and ending with V₂O₅ (top).

transferred wave vector is small compared with the modulus k of the incident wave vector, because the electron collector in a TEM usually has a very small collection angle ($\lesssim 50$ mrad). As a consequence, in most cases, the dimensionless quantity, $\mathbf{q} \cdot \mathbf{r}$, remains small compared with 1, and the main contribution of the exponential, $e^{i\mathbf{q} \cdot \mathbf{r}}$, to the DDSCS comes from the lower terms in its power series expansion. The zeroth order term cancels if the one-electron states ϕ_i and ϕ_f are orthogonal.⁴ The limitation to the first order expansion corresponds to the *dipole approximation* and describes the dipole electric transitions. Under this approximation, the DDSCS is given by:

$$\frac{\partial^2 \sigma}{\partial E \partial \Omega} = \frac{4\gamma^2}{a_0^2 q^4} \sum_{j \text{ unoc}} |\langle \phi_i | \mathbf{q} \cdot \mathbf{r} | \phi_j \rangle|^2 \delta(E_i + E - E_j). \quad (1.28)$$

This expression is similar to the one obtained in the case of XAS, the linear polarization vector of the light being replaced with the momentum transfer $\hbar\mathbf{q}$ (see Chapter 5). Intuitively, from Equation (1.28) one can see the effect of specimen orientation on the measured spectra in the case of an anisotropic sample. The matrix element in Eq. 1.28 is large when the \mathbf{q} wave vector orientation is such that the scalar product $\mathbf{q} \cdot \mathbf{r}$ is maximum in the region where the orbital $\phi_j(\mathbf{r})$ spreads.

Let us assume a very simple case of a highly anisotropic material: hexagonal boron nitride (h-BN) which crystallizes in a graphitic structure. In a simple atomistic picture, the atoms are sp^2 hybridized, and the unoccupied π^* states at lower energy are parallel to the \mathbf{c} axis of the crystal, while the σ^* states at higher energy are in the (\mathbf{a}, \mathbf{b}) planes. The first peak at the edge onset is associated with the π^* atomic orbital which lies along the c -axis, while the second peak is associated with the σ^* atomic orbitals which lie in the (\mathbf{a}, \mathbf{b}) plane. In the case of a forward scattering geometry, \mathbf{q} is parallel to \mathbf{k} . When the incident beam is oriented along the [001] direction of the h-BN crystal, one can expect a dominant contribution of the π^* states, while tilting away from this orientation will increase the relative contribution of the σ^* states. This effect can be seen on the spectra reported in Fig. 1.3

In a more general case, beyond the atomic model, the atomic core wave function is of the form:

$$\phi_i(\mathbf{r}) = R_{n_i \ell_i}(r) Y_{\ell_i m_i}(\hat{\mathbf{r}}). \quad (1.29)$$

In the above expression, $\hat{\mathbf{r}}$ is the unit vector in the direction of \mathbf{r} , and it only depends on the angular spherical coordinates, θ and φ . The valence wave function, $\phi_j(\mathbf{r})$, can be described as a Bloch wave function (the target is represented by an infinite crystal with periodic boundary conditions) or an outgoing scattered wave

⁴ It is not generally true because ϕ_f is a one-electron eigen wave function calculated in the presence of an electron hole at the core energy level E_f , while ϕ_i is a one-electron eigen wave function calculated when the target is in its ground state.

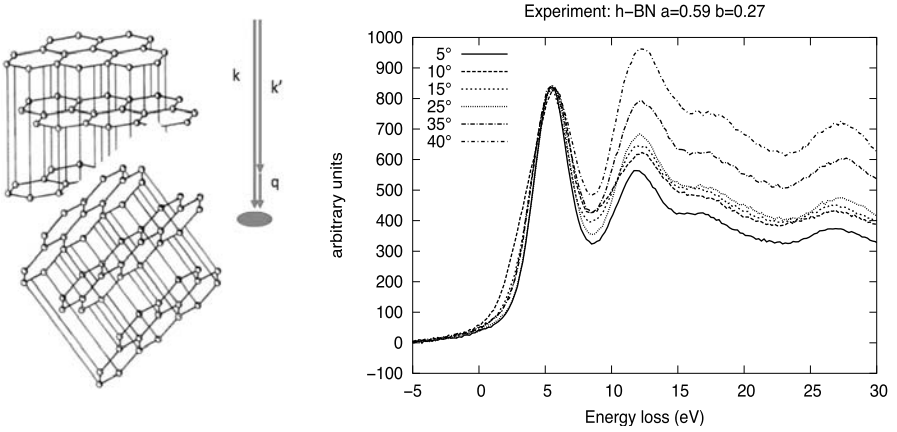


Figure 1.3 B-K edge in h-BN recorded at different specimen orientations and normalized by the π^* peak at 5 eV. The indicated angles denote the angles between the electron beam and the c-axis. At low angles, the π^* peak dominates, while at high angles the σ^* peak dominates.

function calculated in an atomic cluster. Use of the closure relation for the spherical harmonics [Messiah (1958)]:

$$\sum_{\ell m} \sin \theta' Y_{\ell m}(\theta, \varphi) \bar{Y}_{\ell m}(\theta', \varphi') = \delta(\theta' - \theta) \delta(\varphi' - \varphi) \quad (1.30)$$

allows one to establish that, in any case, the valence wave function, $\phi_j(\mathbf{r})$, is of the form

$$\phi_j(\mathbf{r}) = \sum_{\ell_j m_j} R_{j \ell_j m_j}(r) Y_{\ell_j m_j}(\hat{\mathbf{r}}). \quad (1.31)$$

In this relation, $R_{j \ell_j m_j}(r)$ is given by

$$R_{j \ell_j m_j}(r) = \iint_{4\pi} \bar{Y}_{\ell_j m_j}(\theta', \varphi') \phi_j(r, \theta', \varphi') \sin \theta' d\theta' d\varphi' \quad (1.32)$$

The scalar product, $\mathbf{q} \cdot \mathbf{r}$, can also be expressed in terms of spherical harmonics

$$\mathbf{q} \cdot \mathbf{r} = \frac{4\pi qr}{3} \sum_{m=-1}^{m=1} \bar{Y}_{1m}(\hat{\mathbf{q}}) Y_{1m}(\hat{\mathbf{r}}). \quad (1.33)$$

By using the equations 1.29, 1.31 and 1.33, it can be shown that

$$\langle \phi_i | \mathbf{q} \cdot \mathbf{r} | \phi_j \rangle \propto \sum_{m=-1}^{m=1} \bar{Y}_{1m}(\hat{\mathbf{q}}) \iint_{4\pi} \bar{Y}_{\ell_i m_i}(\hat{\mathbf{r}}) Y_{1m}(\hat{\mathbf{r}}) Y_{\ell_j m_j}(\hat{\mathbf{r}}) \sin \theta d\theta d\varphi. \quad (1.34)$$

In the above expression, the integral is a Gaunt coefficient. According to the properties of these coefficients, necessary conditions to obtain a non zero matrix element are

$$-m_i + m + m_j = 0 \quad (1.35a)$$

$$\ell_i + 1 + \ell_j \text{ is even} \quad (1.35b)$$

$$|\ell_i - 1| \leq \ell_j \leq |\ell_i + 1|. \quad (1.35c)$$

Both latter relations are summarized in

$$\ell_j = \ell_i \pm 1 \quad \text{and} \quad \ell_j \geq 0 \quad (1.36)$$

which represents *the dipole selection rule*. This selection rule means that, in the case of a $1s$ atomic core state (K edge, $n_i = 1$), the only possible transition are s to p transitions, in the case of a $2p$ atomic core state (L_2 or L_3 edge, $n_i = 2$), the only possible transitions are p to d or p to s transitions, etc. Obviously, the transitions are governed by the dipole selection rule only if the dipole approximation is valid.

Because of dynamical diffraction, the description of the ELNES when the sample is crystalline is more complicated. The fast electron may scatter elastically both before and after the inelastic event. The elastic scattering is described by dynamical diffraction theory, which will be discussed in detail in Chapter 11. The inelastic signal will then contain contributions from several coherently excited Bragg waves which may interfere. For example, if the Ewald sphere intersects only two diffraction spots corresponding to the reciprocal lattice vector $\mathbf{0}$ and \mathbf{g} , then we can have

$$\mathbf{k}' = \mathbf{k} + \mathbf{q} = \mathbf{k} + \mathbf{g} + \mathbf{q}'.$$

In this case, the reduced density matrix Eq. (1.9) shows off-diagonal elements

$$\langle \mathbf{k} + \mathbf{q} | \rho_k | \mathbf{k} + \mathbf{g} + \mathbf{g} \rangle$$

which contribute to the measured signal. These terms are described by an extension of the definition of the DDF by expression 1.26 called the mixed dynamic form factor (MDFF):

$$S(\mathbf{q}, \mathbf{q}', E) = \sum_{j \text{ unoc}} \langle \phi_i | e^{i\mathbf{q}\cdot\mathbf{r}} | \phi_j \rangle \langle \phi_j | e^{-i\mathbf{q}'\cdot\mathbf{r}} | \phi_i \rangle \delta(E_j - E_i - E). \quad (1.37)$$

In addition, the quantities $\mathbf{q} \cdot \mathbf{r}$ and $\mathbf{q}' \cdot \mathbf{r}$ might be close to 1 and the standard dipole approximation $e^{i\mathbf{q}\cdot\mathbf{r}} \approx 1 + i\mathbf{q} \cdot \mathbf{r}$, is no longer valid. It is then better to use the Rayleigh expansion

$$e^{i\mathbf{q}\cdot\mathbf{r}} \approx j_0(qr) + \frac{3i\mathbf{q} \cdot \mathbf{r}}{qr} j_1(qr) \quad (1.38)$$

which has a correct asymptotic behaviour for large \mathbf{q} vectors. In the above expression, $j_0(kr)$ and $j_1(kr)$ are spherical Bessel functions. To complete the description of the DFT calculations of ELNES spectra one needs to describe the movement of the electron beam through the sample. This topic is discussed in Chap. 14.

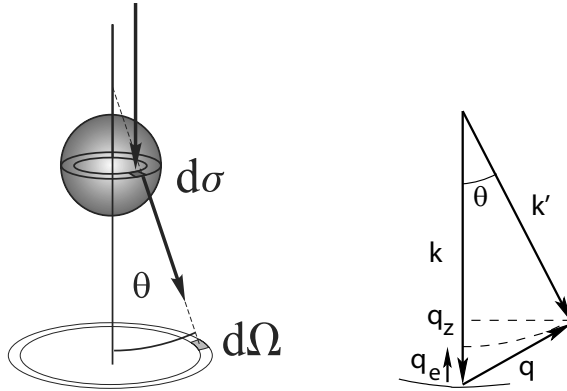


Figure 1.4 Scattering geometry: (a) Differential cross section; (b) scattering diagram for inelastic processes.

1.6 SCATTERING KINEMATICS

The DDSCS is the area $d\sigma$ of the scatterer that the probe electron encounters during an inelastic interaction process Fig. 1.4(a). The relation between Ω and \mathbf{q} is given by the scattering geometry, Fig. 1.4(b).

Applying the cosine law to the scattering triangle in Fig. 1.4(b), we obtain the relationship between wavenumber transfer, q , and the scattering angle, θ :

$$q^2 = k^2 + k'^2 - 2kk' \cos \theta. \quad (1.39)$$

For small θ the cosine can be expanded as $\cos \theta \simeq 1 - \theta^2/2$, and

$$q^2 \simeq k^2 + k'^2 - 2kk' + kk'\theta^2 = q_e^2 + kk'\theta^2 \quad (1.40)$$

with $q_e = k - k'$ the difference of wavenumbers k and k' , that is to say before and after the scattering process. In Fig. 1.4(b), q_z is the component of \mathbf{q} parallel to the incident beam. As the energy losses E are very small compared with the kinetic energy of the fast incident electron, initial and final wavenumbers are very close, and thus

$$q^2 \simeq q_e^2 + k^2\theta^2 \quad (1.41)$$

and at very low incidence angles the wavenumber q approaches q_e :

$$\lim_{\theta \rightarrow 0} q = q_e.$$

Equation (1.25) tells us that the DDSCS is the product of a kinematic part ($4\gamma^2/a_0^2q^4$) and the DFF.

It is interesting to compare the behaviour of the DDSCS with that of the *elastic* cross section which can be written in the form [Schattschneider (1986)].

$$\frac{d\sigma_{el}}{d\Omega} = \frac{4}{a_0^2q^4} |F(\mathbf{q})|^2. \quad (1.42)$$